

Supplementary Information

CoX₂Y₄: A Family of Two-Dimensional Magnets with Versatile Magnetic Order

Ziyuan Zhao^{*ab}, Zhao Liu^{ab}, Mark T. Edmonds^{bc} and Nikhil V. Medhekar^{*ab}

^a *Department of Materials Science and Engineering, Monash University, Clayton, Victoria 3800, Australia. E-mail: ziyuan.zhao@monash.edu; nikhil.medhekar@monash.edu*

^b *ARC Centre of Excellence in Future Low-Energy Electronics Technologies FLEET, Monash University, Clayton, Victoria 3800, Australia.*

^c *School of Physics and Astronomy, Monash University, Clayton, Victoria 3800, Australia.*

Table of Contents

1. Computational Details.....	2
2. Supporting Figures	7
3. Supporting Tables	14
4. References	17

1. Computational Details

We performed structural optimization, magnetic properties and thermal stabilities calculations for CoX_2Y_4 SLs by using density functional theory (DFT) ¹ within the generalized gradient approximation (GGA) ² as implemented in the VASP code ^{3,4}. A vacuum of ~ 15 Å was used to avoid interaction between adjacent layers. The cut-off energy for the expansion of wavefunctions into plane waves was set to 500 eV in all calculations. The Monkhorst-Pack k mesh of $12 \times 12 \times 1$ was used to yield a good convergence. All structural optimizations were performed using a conjugate-gradient algorithm and a force tolerance criterion for convergence of 0.01 eV/Å. The energy convergence criterion was set to 10^{-6} eV providing well-converged total energies of different magnetic configuration. Spin-orbit coupling was considered for calculating magneto-crystalline anisotropy energies (MAE) and confirming the easy axis ⁵. Phonon dispersions were calculated in the Phonopy code, where the force constants were obtained from DFT calculations based on the supercell approach ⁶.

The Hubbard U parameter plays a crucial role in adjusting the effective on-site electron-electron interaction within Co $3d$ -states^{7,8}, thus impacting the ground magnetic state. To evaluate the robustness of the ground magnetic states of CoX_2Y_4 SLs, we extensively tested different effective U values in the Dudarev's scheme and different J values (0 – 1 eV) with $U = 4$ eV in Liechtenstein's scheme. The energy differences between collinear antiferromagnetic (*c*AFM), non-collinear antiferromagnetic (*ncl*AFM) and non-coplanar antiferromagnetic states (*n*cpAFM) relative to the ferromagnetic (FM) state of CoX_2Y_4 SLs at different U and J values are depicted in Fig. SI and SII. Across a wide range of U and J values, CoBi_2Te_4 remains *ncl*AFM as the ground magnetic state, and *c*AFM is the ground state for $\text{CoBi}_2\text{Se}_2\text{Te}_2$, CoBi_2Se_4 and CoSb_2Te_4 . Our rigorous testing of U confirms the robustness of the ground magnetic states of CoX_2Y_4 . Given that a U value of 4 eV was employed to analyze the magnetic and electronic properties of MnBi_2Te_4 and NiBi_2Te_4 ⁹, and considering CoX_2Y_4 shares isostructural similarity with MnBi_2Te_4 -family materials, as well as the fact that Co, Mn and Ni belong to the same transition metal group in the periodic table, we opted for an effective U of 4 eV in Dudarev's scheme for CoX_2Y_4 . As our comprehensive testing shows, this choice is dependable and highlights the importance of our findings regarding CoX_2Y_4 SLs compared to other materials within the MnBi_2Te_4 family.

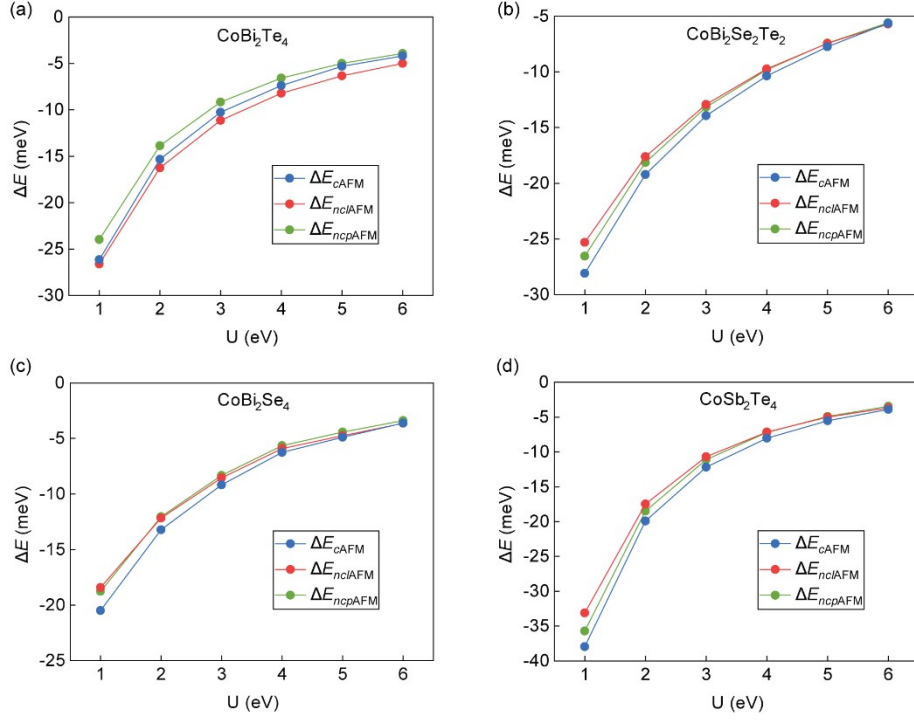


Fig. SI Energy difference per formula unit between different magnetic states for CoX_2Y_4 SLs as a function of different U_{eff} values in Dudarev's scheme.

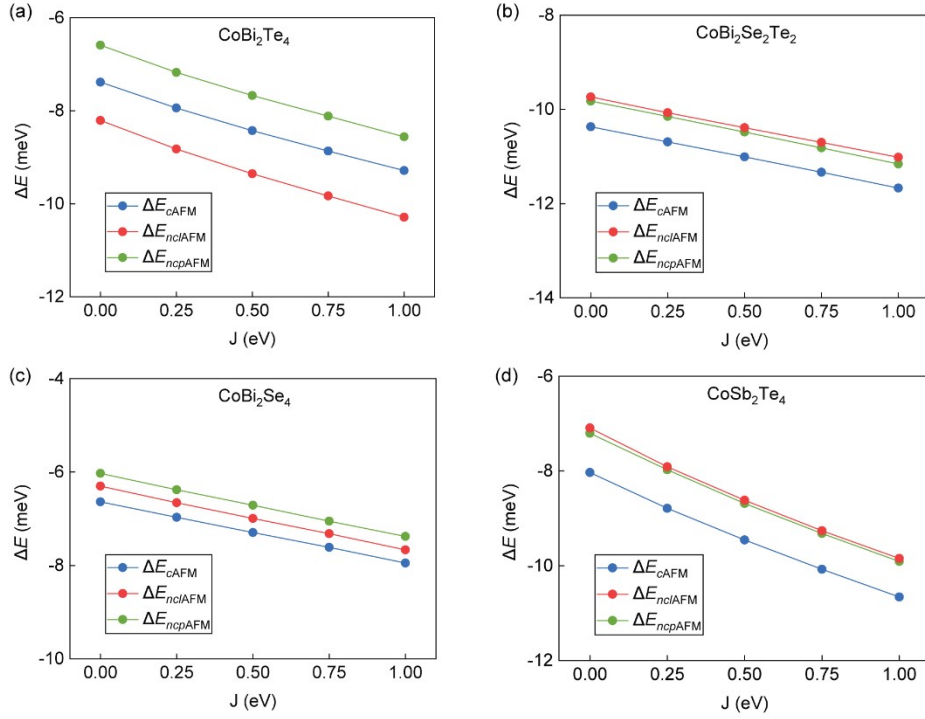


Fig. SII Energy difference per formula unit between different magnetic states for CoX_2Y_4 SLs as a function of different J values with $U = 4$ eV in Liechtenstein's scheme.

The cohesive energies E^c of the CoX_2Y_4 SLs were calculated by using the following formula,

$$E^c = (E_{\text{Co}} + 2E_{\text{X}} + 4E_{\text{Y}} - E_{\text{CoX}_2\text{Y}_4})/7$$

where E_{Co} , E_{X} , E_{Y} , and $E_{\text{CoX}_2\text{Y}_4}$ are the total energies of one Co atom, one Bi or Sb atom, one Te or Se atom, and one unit cell of the CoBi_2Te_4 SL.

To search the magnetic ground state, we built a *c*AFM configuration of 2×2 in-plane supercells containing four Co atoms per SL, a triangular *ncl*AFM configuration of $\sqrt{3} \times \sqrt{3}R30^\circ$ in-plane supercells containing three Co atoms per SL, and a non-coplanar antiferromagnetism (*ncp*AFM) configuration of 2×2 in-plane supercells containing four Co atoms per SL. The Monkhorst–Pack *k*-mesh of $7 \times 7 \times 1$ and $6 \times 6 \times 1$ were selected for the calculations of $\sqrt{3} \times \sqrt{3}R30^\circ$ and 2×2 supercells, respectively. And magnetic anisotropy energies were calculated by using dense *k*-point meshes of $18 \times 18 \times 1$.

To estimate exchange coupling parameters based on 2D Heisenberg model, we define a spin Hamiltonian as,

$$\hat{H} = E_0 - \sum_{\langle ij \rangle} J_1 \vec{S}_i \cdot \vec{S}_j - \sum_{\langle\langle ij \rangle\rangle} J_2 \vec{S}_i \cdot \vec{S}_j$$

where J_1 and J_2 are the exchange coupling parameters between nearest and next-nearest neighbour Co atoms, E_0 is the reference energy, the summation $\langle ij \rangle$ runs over all nearest neighbour Co sites, and the summation $\langle\langle ij \rangle\rangle$ runs over all next-nearest neighbour Co sites. Since the *d*-electrons of Co of CoX_2Y_4

form a high spin state, we used $S = \frac{3}{2}$ for Co. The exchange parameters J_1 and J_2 can be derived from the mapping analysis of different spin configurations. We built three different spin configurations, i.e., FM, *c*AFM and *ncl*AFM, within six-fold unit cells, as shown in Fig. SIII.

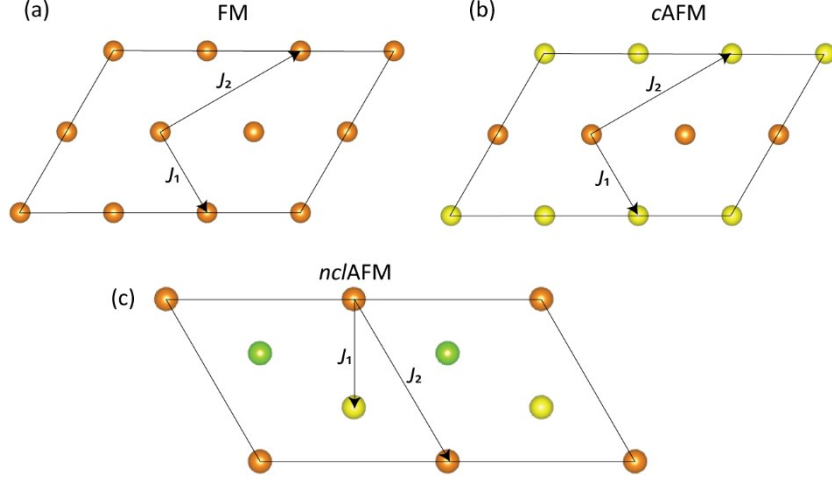


Fig. SIII The top view of Co atoms in FM (a), *cAFM* (b) and *nclAFM* (c) configurations within six-fold unit cells. The different colours of Co atoms represent different spin orientations.

By counting the nearest and next-nearest neighbour Co atom pairs, we know that there are 18 nearest neighbour pairs and 18 next-nearest neighbour pairs. For the FM configuration, S_i and S_j are same, the spin Hamiltonian can be written as

$$E_{\text{FM}} = E_0 - 18J_1S^2 - 18J_2S^2 \quad (1)$$

In the *cAFM* configuration, 6 spin pairs of 18 pairs have the same sign, and the other 12 pairs have different signs for both nearest and next-nearest neighbour Co atoms. The total energy of *cAFM* is

$$E_{\text{cAFM}} = E_0 + 6J_1S^2 + 6J_2S^2 \quad (2)$$

For the *nclAFM* configuration, there are three kinds of Co atoms with different in-plane spin orientations, and the spin orientations are not collinear. We can label them as S_1 , S_2 and S_3 and define the spin orientation by describing components on the x and y axis, as:

$$S_{1x} = -S\cos30^\circ, S_{1y} = S\sin30^\circ, S_{2x} = S\cos30^\circ, S_{2y} = S\sin30^\circ, S_{3x} = S\cos90^\circ, \text{ and } S_{3y} = -S\sin90^\circ$$

The spin Hamiltonian of *nclAFM* configuration is thus,

$$E_{\text{nclAFM}} = E_0 - 6J_1[(S_{1x}S_{2x} + S_{1x}S_{3x} + S_{2x}S_{3x}) + (S_{1y}S_{2y} + S_{1y}S_{3y} + S_{2y}S_{3y})] - 6J_2[(S_{1x}S_{1x} + S_{2x}S_{2x} + S_{3x}S_{3x}) + (S_{1y}S_{1y} + S_{2y}S_{2y} + S_{3y}S_{3y})]$$

$$E_{\text{nclAFM}} = E_0 + 9J_1S^2 - 18J_2S^2 \quad (3)$$

From equations (1), (2) and (3), we obtain J_1 and J_2 for all CoX_2Y_4 SLs.

Monte Carlo simulations were performed using a 32×32 supercell containing 1024 spin sites. During the simulations, each spin rotates randomly in all directions. The critical temperature was finally obtained from the peak in the magnetic heat capacity.

We include the dipole-dipole interaction energies on both in-plane and out-of-plane magnetization directions to obtain the MAE with the dipole-dipole corrections for CoX_2Y_4 SLs. The dipole-dipole interaction energy can be expressed as:

$$E_{\text{dd}} = \frac{1}{N} \frac{\mu_0}{4\pi} \sum_{i \neq j}^N \left[\frac{\vec{M}_i \cdot \vec{M}_j}{r_{ij}^3} - \frac{3(\vec{M}_i \cdot \vec{r}_{ij})(\vec{M}_j \cdot \vec{r}_{ij})}{r_{ij}^5} \right]$$

2. Supporting Figures

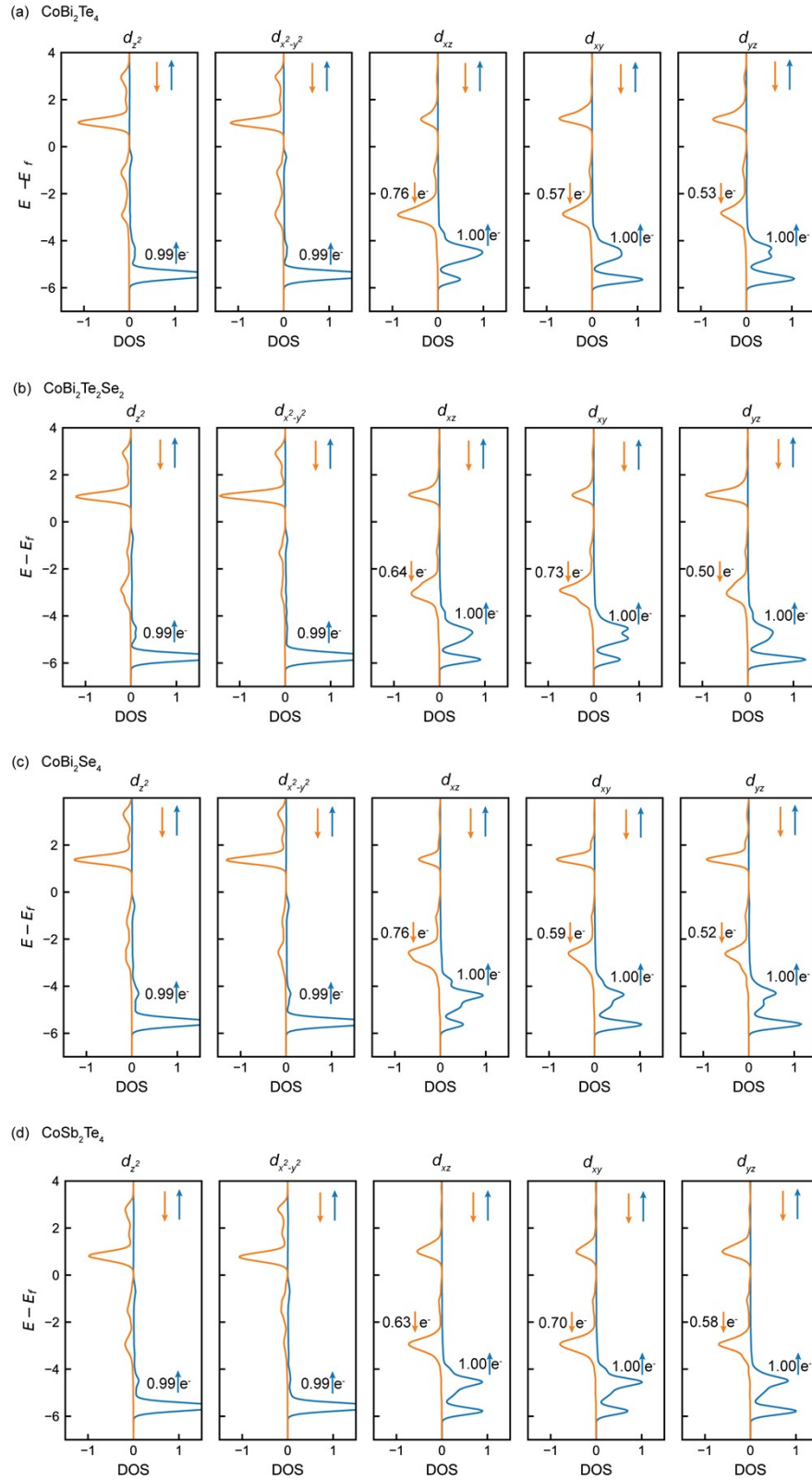


Fig. S1 The projected density of states (PDOS) for the d -orbitals of Co atom in CoX_2Y_4 SLs. The integrated PDOS of spin-up state on each d -orbital is ~ 1 eV, indicating each d -orbital is occupied by one spin-up electron. Another two electrons fractionally occupy the three degenerate t_{2g} orbitals with lower energy.

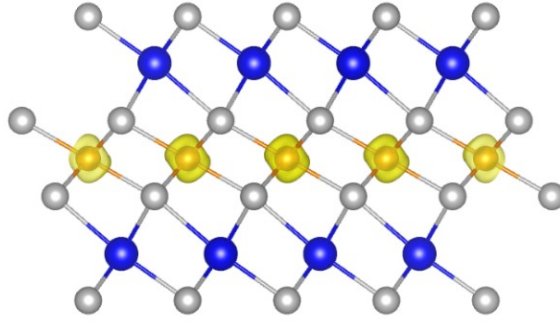


Fig. S2 Spin density distribution of CoBi_2Te_4 with an isosurface value of 0.03 au. The spin density is concentrated around the Co atoms, indicating that Co provides the magnetism.

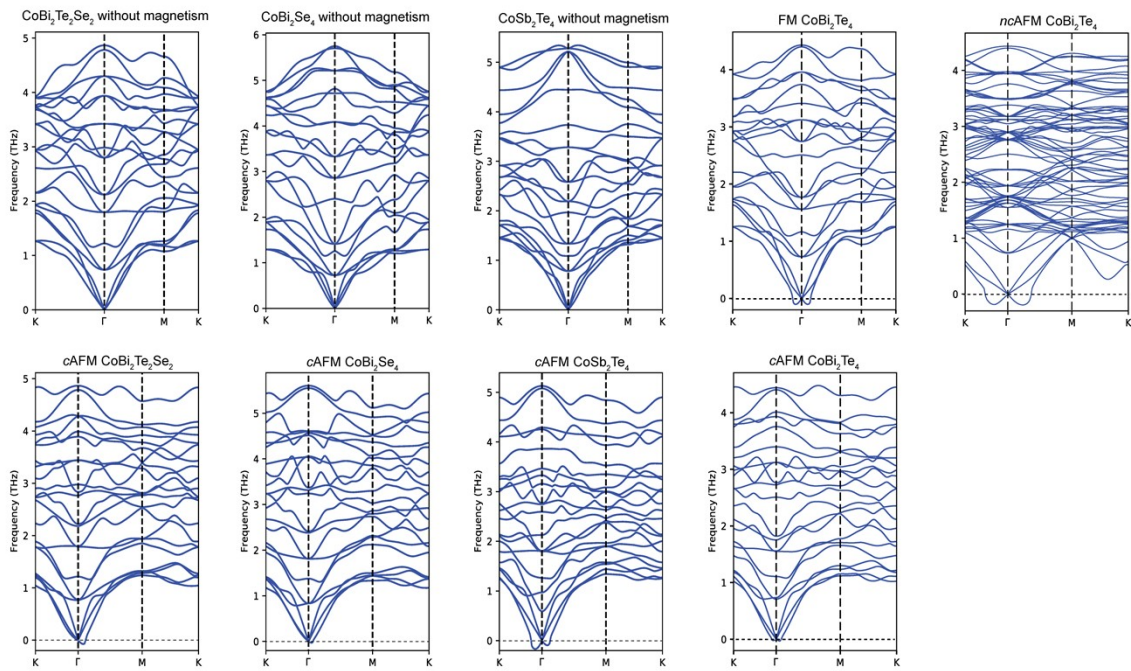


Fig. S3 The phonon spectra of $\text{CoBi}_2\text{Te}_2\text{Se}_2$, CoBi_2Se_4 , CoSb_2Te_4 , and CoBi_2Te_4 SLs. The small negative phonon frequencies observed in the acoustic branches near the Γ point stem from minor numerical inaccuracies, which slightly break the continuous translational invariance of a solid.

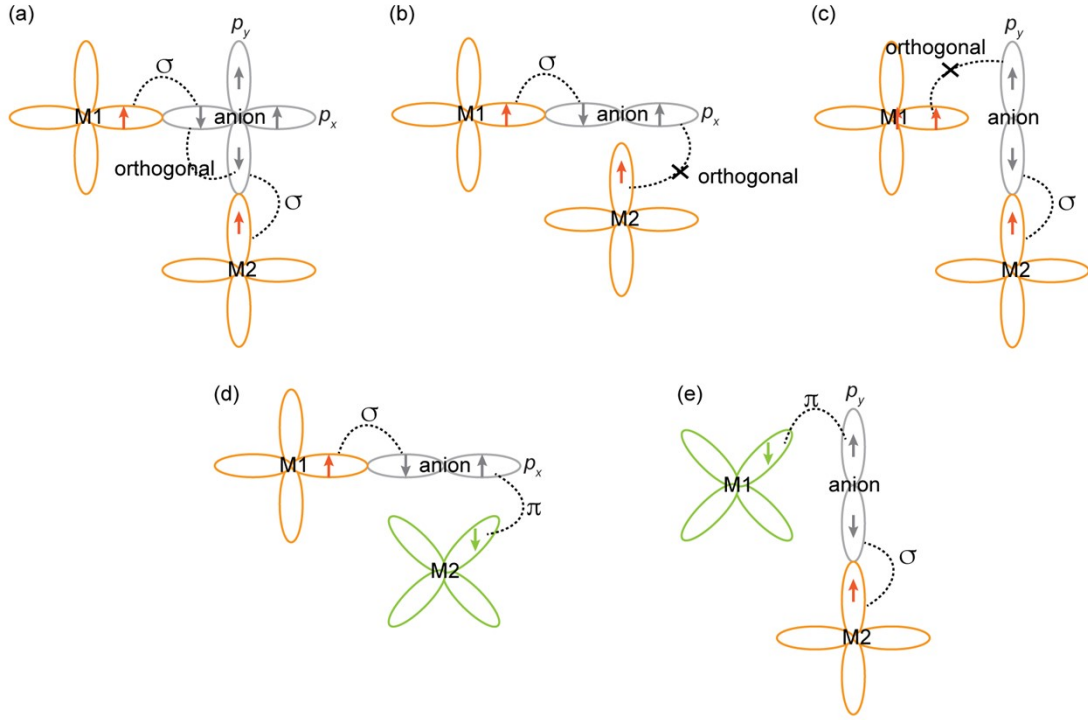


Fig. S4 (a-c) The 90° ferromagnetic superexchange interaction explained by Goodenough-Kanamori-Anderson rules. (d, f) The 90° antiferromagnetic superexchange channels consisting of σ and π -bond orbital overlap.

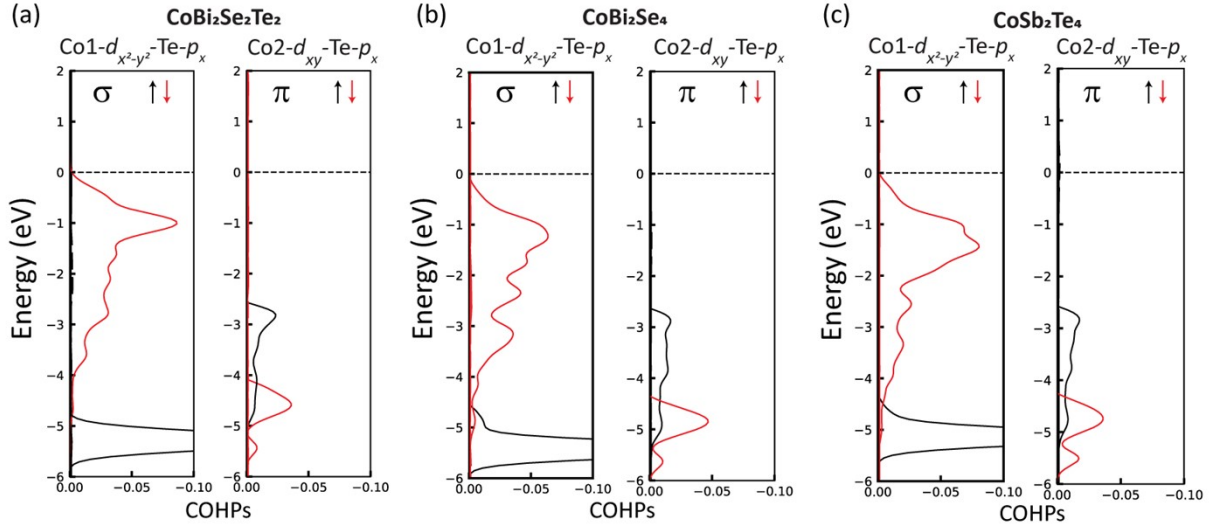


Fig. S5 COHPs of overlap between (a) $\text{Co1-}d_{x^2-y^2}-\text{Te-}p_x$ orbitals and $\text{Co2-}d_{xz}-\text{Se-}p_x$ orbitals in $\text{CoBi}_2\text{Se}_2\text{Te}_2$ SL, (b) $\text{Co1-}d_{x^2-y^2}-\text{Se-}p_x$ orbitals and $\text{Co2-}d_{xz}-\text{Se-}p_x$ orbitals in CoBi_2Se_4 SL, and (c) $\text{Co1-}d_{x^2-y^2}-\text{Te-}p_x$ orbitals and $\text{Co2-}d_{xz}-\text{Te-}p_x$ orbitals in CoSb_2Te_4 SL. The strength of the σ and π bond in all cases is comparable to that of CoBi_2Te_4 , leading to the antiferromagnetic coupling.

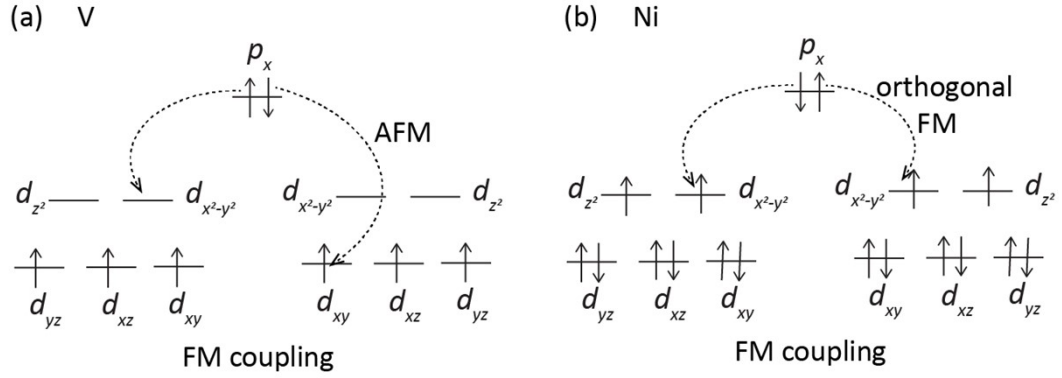


Fig. S6 (a) Schematics of ferromagnetic superexchange interaction between V1- $d_{x^2-y^2}$ -Te- p_x and V2- d_{xy} -Te- p_x in the VBi₂Te₄ septuple layer. The $d_{x^2-y^2}$ -orbital of V is empty, which allows the hopping of spin-up electrons of Te- p_x orbital. And the remaining spin-down electron will not shift the spin-up electron of the d_{xy} orbital of the other V. Thus, it forms a ferromagnetic coupling. (b) Schematic of ferromagnetic superexchange interaction between Ni1- $d_{x^2-y^2}$ -Te- p_x and Ni2- d_{xy} -Te- p_x in the NiBi₂Te₄ septuple layer. The d_{xy} orbital in Ni is fully occupied, which cannot accommodate extra electrons; and the Te- p_x is orthogonal to the $d_{x^2-y^2}$ -orbital of the other Ni, leading to a ferromagnetic coupling.

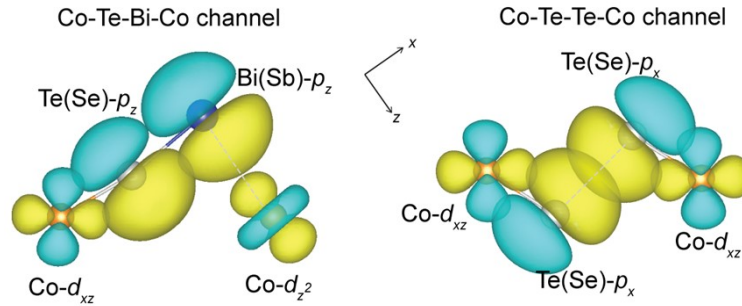


Fig. S7 The Co- d_{xz} -Te(Se)- p_z -Bi(Sb)- p_z -Co- d_{z^2} and Co- d_{xz} -Te(Se)- p_x -Te(Se)- p_x -Co- d_{xz} superexchange channels with orbital shapes. The orbitals are rotated according to local chemical bonds, which are linear arranged along the x and z axis.

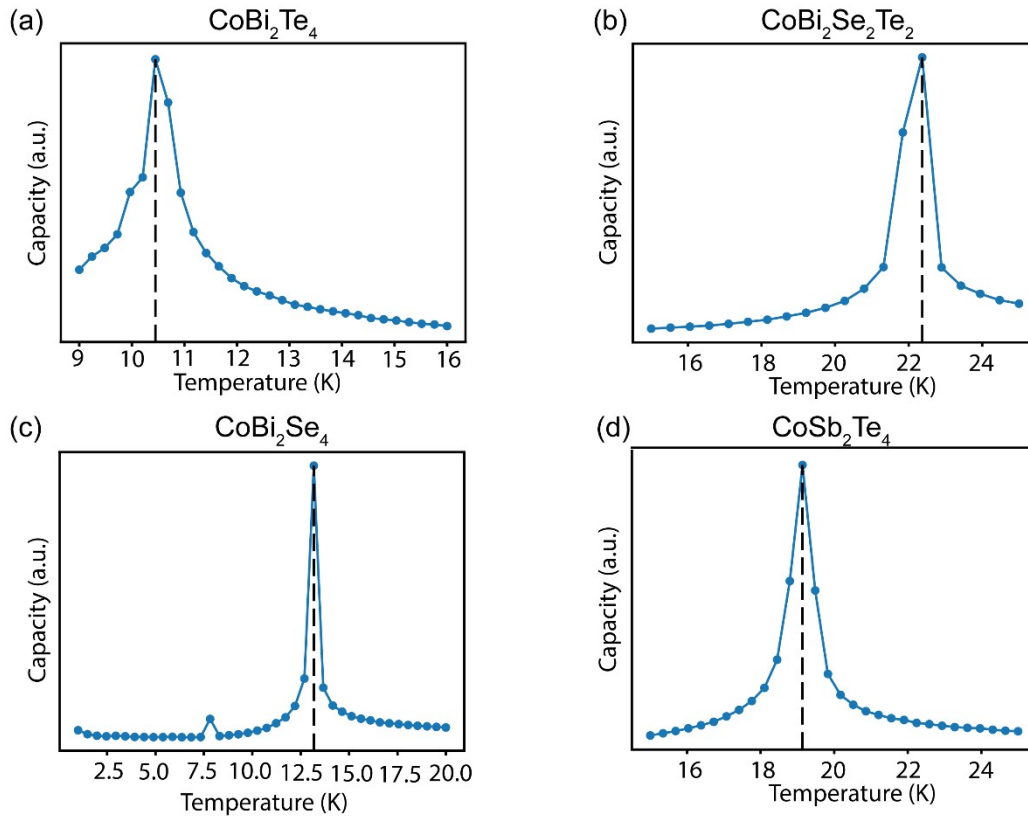


Fig. S8 Magnetic capacities of CoBi_2Te_4 (a), $\text{CoBi}_2\text{Se}_2\text{Te}_2$ (b), CoBi_2Se_4 (c), and CoSb_2Te_4 (d) SLs from Monte Carlo simulation. The dashed line represents the N^{el} temperature.

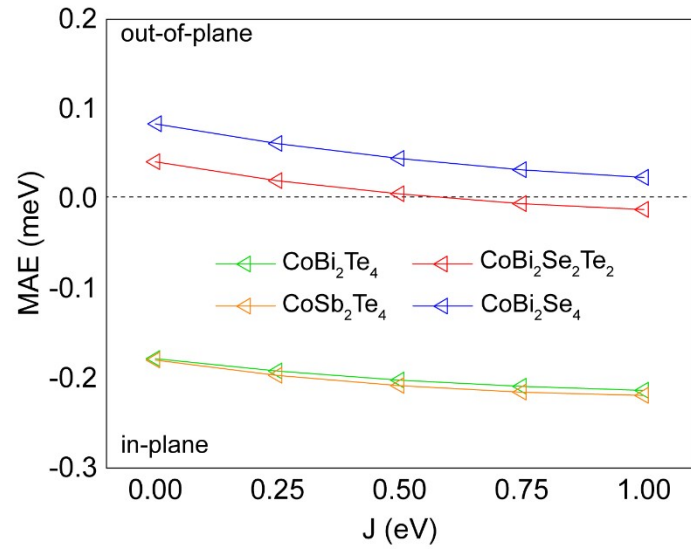


Fig. S9 The MAE for CoX_2Y_4 SLs as a function of different J values with $U = 4$ eV in Liechtenstein's scheme. ($\text{MAE} = E_{\text{in-plane}} - E_{\text{out-of-plane}}$)

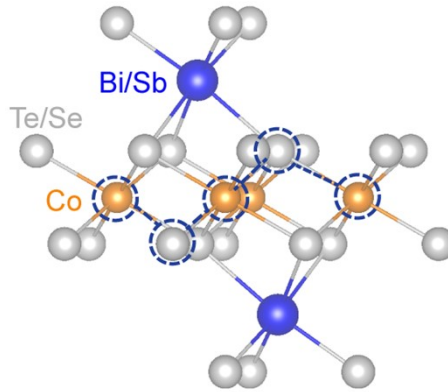


Fig. S10 The FM super-superexchange coupling via Co-Te(Se)-Co-Te(Se)-Co channel.

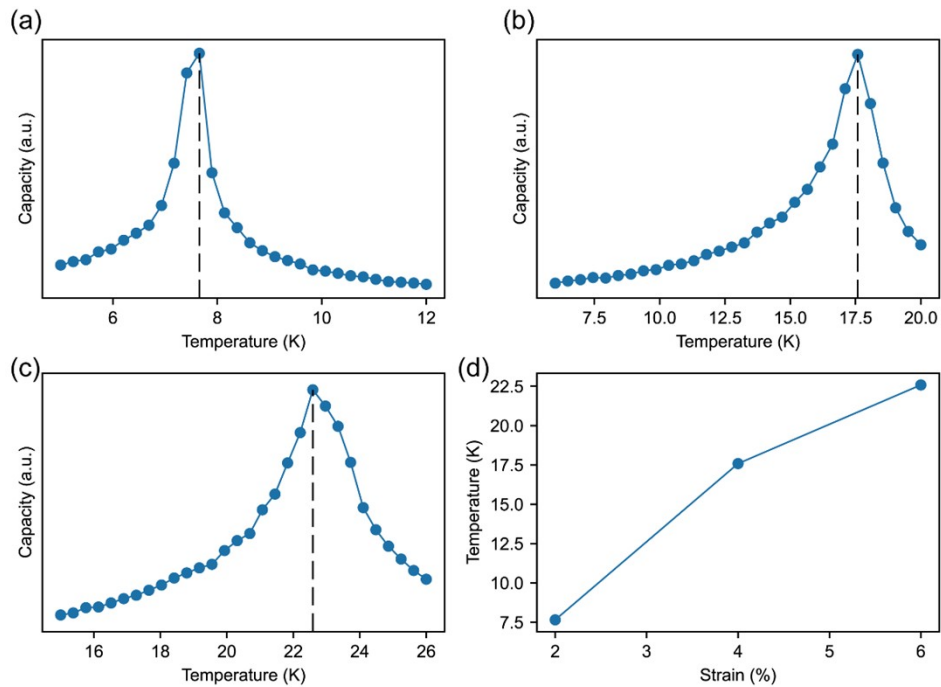


Fig. S11 Magnetic capacities of the *nclAFM* state of CoSb_2Te_4 SL under the biaxial strains of 2% (a), 4% (b) and 6% (c). (d) The change of N^{el} temperatures as a function of biaxial strain.

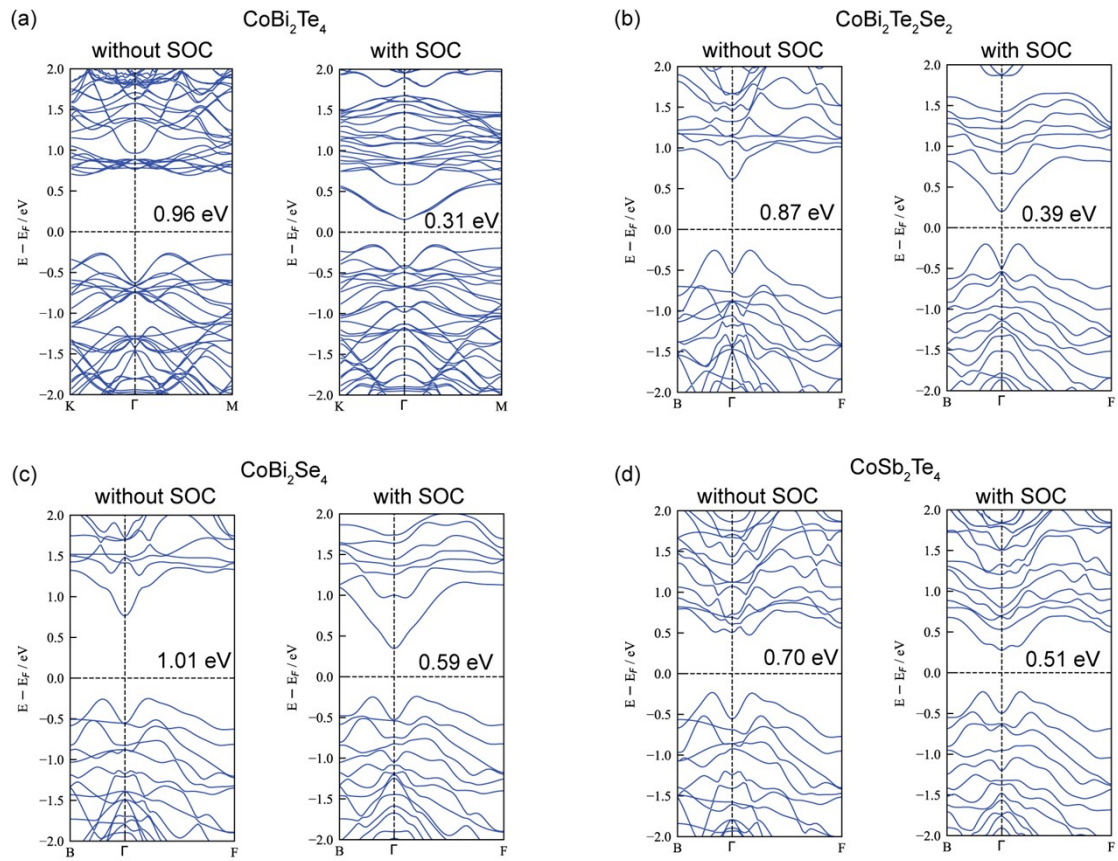


Fig. S12 The band structures of *nIAFM* CoBi_2Te_4 (a), *cAFM* $\text{CoBi}_2\text{Te}_2\text{Se}_2$ (b), *cAFM* CoBi_2Se_4 (c), and *cAFM* CoSb_2Te_4 (d) SLs without and with spin-orbital coupling, respectively.

3. Supporting Tables

Table S1. Structural information for CoX_2Y_4 SLs.

	Lattice Parameter $a = b$ (Å)	Thickness (Å)	Angle Co/Mn- Te/Se-Co/Mn (°)	Cohesive Energy (eV/atom)
CoBi_2Te_4 SL	4.33	10.70	97.54	3.10
$\text{CoBi}_2\text{Se}_2\text{Te}_2$ SL	4.18	10.22	99.62	3.26
CoBi_2Se_4 SL	4.07	9.95	98.08	3.43
CoSb_2Te_4 SL	4.26	10.44	96.66	3.07
MnBi_2Te_4 SL	4.38	10.93	94.18	2.77

Table S2. Bond lengths in CoX_2Y_4 SLs.

	Co-Te(Se) (Å)	Te(Se)-Te(Se) (Å)	Te(Se)-Bi(Sb) (Å)	Bi(Sb)-Co (Å)
CoBi_2Te_4	2.88	3.79	3.31	4.38
$\text{CoBi}_2\text{Se}_2\text{Te}_2$	2.74	3.53	3.13	4.07
CoBi_2Se_4	2.70	3.54	3.12	4.11
CoSb_2Te_4	2.85	3.79	3.22	4.30

Table S3. The total energies of the high-spin ($E_{S=3/2}$) and low-spin ($E_{S=1/2}$) states of Co in CoX_2Y_4 SLs.

	$E_{S=3/2}$ (eV/f.u.)	$E_{S=1/2}$ (eV/f.u.)
CoBi_2Te_4	-25.77	-25.31
$\text{CoBi}_2\text{Se}_2\text{Te}_2$	-27.17	-26.48
CoBi_2Se_4	-28.55	-27.82

CoSb ₂ Te ₄	-25.80	-25.47
-----------------------------------	--------	--------

Table S4. The formation energies of CoX₂Y₄ SLs relative to elemental solids. The formation energies E^f were calculated by using the formula, $E^f = (E_{CoX_2Y_4} - E_{Co} + 2E_X + 4E_Y)/7$, where $E_{CoX_2Y_4}$ is the total energy of one unit cell of the CoBi₂Te₄ SL. E_{Co} , E_X , and E_Y are the energies per atom of $Fm\bar{3}m$ Co, $R\bar{3}m$ Bi, $R\bar{3}m$ Sb, $P3_121$ Te, and $P3_121$ Se.

	Formation energy (eV/atom)
CoBi ₂ Te ₄ SL	-0.21
CoBi ₂ Se ₂ Te ₂ SL	-0.31
CoBi ₂ Se ₄ SL	-0.40
CoSb ₂ Te ₄ SL	-0.13

Table S5. The energy difference between different magnetic configurations for CoX₂Y₄ SLs, obtained by considering SOC ($\Delta E_{cAFM} = E_{cAFM} - E_{FM}$; $\Delta E_{nclAFM} = E_{nclAFM} - E_{FM}$; $\Delta E_{ncpAFM} = E_{ncpAFM} - E_{FM}$), meV per unit cell.

	ΔE_{cAFM}	ΔE_{nclAFM}	ΔE_{ncpAFM}
CoBi ₂ Te ₄	-6.87	-7.61	-5.56
CoBi ₂ Se ₂ Te ₂	-10.27	-9.88	-9.89
CoBi ₂ Se ₄	-6.21	-6.17	-5.69
CoSb ₂ Te ₄	-7.37	-6.44	-5.97

Table S6. The hopping energies of the Co-Te(Se)-Bi(Sb)-Co and Co-Te(Se)-Te(Se)-Co super-superexchange couplings. $\tau_{\text{Co-Te(Se)-Bi(Sb)-Co}} = \tau_{\text{Co-Te(Se)}}\tau_{\text{Te(Se)-Bi(Sb)}}\tau_{\text{Bi(Sb)-Co}}$; $\tau_{\text{Co-Te(Se)-Te(Se)-Co}} = \tau_{\text{Co-Te(Se)}}\tau_{\text{Te(Se)-Te(Se)-Co}}$; $\tau_{\text{eff}} = \tau_{\text{Co-Te(Se)-Bi(Sb)-Co}} + \tau_{\text{Co-Te(Se)-Te(Se)-Co}}$

	$\tau_{\text{Co-Te(Se)}}\text{ (eV)}$	$\tau_{\text{Te(Se)-Bi(Sb)}}\text{ (eV)}$	$\tau_{\text{Te(Se)-Te(Se)}}\text{ (eV)}$	$\tau_{\text{Bi(Sb)-Co}}\text{ (eV)}$	$\tau_{\text{Co-Te(Se)-Bi(Sb)-Co}}\text{ (eV)}$	$\tau_{\text{Co-Te(Se)-Te(Se)-Co}}\text{ (eV)}$	$\tau_{\text{eff}}\text{ (eV)}$
CoBi ₂ Te ₄	0.23	0.29	1.07	0.04	0.0027	0.0566	0.0593
CoBi ₂ Se ₂ Te ₂	0.25	0.32	0.95	0.12	0.0096	0.0594	0.0690
CoBi ₂ Se ₄	0.24	0.34	0.96	0.09	0.0073	0.0553	0.0626
CoSb ₂ Te ₄	0.25	0.30	1.09	0.04	0.0030	0.0681	0.0711

Table S7. The magnetic anisotropy energy (MAE) per Co ($\text{MAE} = E_{\text{in-plane}} - E_{\text{out-of-plane}}$). MAE_{soc} is the MAE with spin-orbital coupling, MAE_{dd} is the MAE with dipole-dipole corrections, and $\text{MAE}_{\text{total}}$ contains the joint effects of SOC and dipole-dipole corrections.

	$\text{MAE}_{\text{soc}}\text{ (meV)}$	$\text{MAE}_{\text{dd}}\text{ (meV)}$	$\text{MAE}_{\text{total}}\text{ (meV)}$
CoBi ₂ Te ₄ SL	-0.177	0.006	-0.171
CoBi ₂ Se ₂ Te ₂ SL	0.041	0.007	0.048
CoBi ₂ Se ₄ SL	0.084	0.008	0.092
CoSb ₂ Te ₄ SL	-0.180	0.007	-0.173

4. References

- 1 W. Kohn and L. J. Sham, *Phys. Rev.*, 1965, **140**, A1133–A1138.
- 2 J. P. Perdew, K. Burke and M. Ernzerhof, *Phys. Rev. Lett.*, 1996, **77**, 3865–3868.
- 3 G. Kresse and J. Furthmüller, *Phys. Rev. B*, 1996, **54**, 11169–11186.
- 4 G. Kresse and D. Joubert, *Phys. Rev. B*, 1999, **59**, 1758–1775.
- 5 D. D. Koelling and B. N. Harmon, *J. Phys. C: Solid State Phys.*, 1977, **10**, 3107.
- 6 A. Togo, F. Oba and I. Tanaka, *Phys. Rev. B*, 2008, **78**, 134106.
- 7 S. Grimme, J. Antony, S. Ehrlich and H. Krieg, *J. Chem. Phys.*, 2010, **132**, 154104.
- 8 S. Grimme, S. Ehrlich and L. Goerigk, *Journal of Computational Chemistry*, 2011, **32**, 1456–1465.
- 9 J. Li, Y. Li, S. Du, Z. Wang, B.-L. Gu, S.-C. Zhang, K. He, W. Duan and Y. Xu, *Science Advances*, 2019, **5**, eaaw5685.